**Kunpeng Wang**[1]
School of Naval Architecture
and Ocean Engineering,
Jiangsu University of Science and Technology,
Zhenjiang 212003, Jiangsu, China
e-mail: jstuwk@sina.com

**Chunyan Ji**
School of Naval Architecture
and Ocean Engineering,
Jiangsu University of Science and Technology,
Zhenjiang 212003, Jiangsu, China

**Hongxiang Xue**
State Key Laboratory of Ocean Engineering,
Shanghai Jiao Tong University,
Shanghai 200240, China

**Wenyong Tang**
State Key Laboratory of Ocean Engineering,
Shanghai Jiao Tong University,
Shanghai 200240, China

# Fatigue Damage Study of Helical Wires in Catenary Unbonded Flexible Riser Near Touchdown Point

*This study presents an analytical model of flexible riser and implements it into finite-element software* ABAQUS *to investigate the fatigue damage of helical wires near touchdown point (TDP). In the analytical model, the interlayer contact pressure is simulated by setting up springs between adjacent interlayers. The spring stiffness is iteratively updated based on the interlayer penetration and separation conditions in the axisymmetric analysis. During the bending behavior, the axial stress of helical wire along the circumferential direction is traced to determine whether the axial force overcomes the interlayer friction force and thus lead to sliding. Based on the experimental data in the literature, the model is verified. The present study implements this model into* ABAQUS *to carry out the global analysis of the catenary flexible riser. In the global analysis, the riser–seabed interaction is simulated by using a hysteretic seabed model in the literature. The effect of the seabed stiffness and interlayer friction on the fatigue damage of helical wire near touchdown point is parametrically studied, and the results indicate that these two aspects significantly affect the helical wire fatigue damage, and the sliding of helical wires should be taken into account in the global analysis for accurate prediction of fatigue damage. Meanwhile, different from the steel catenary riser, high seabed stiffness may not correspond to high fatigue damage of helical wires.* [DOI: 10.1115/1.4036675]

*Keywords: unbonded flexible riser, helical wire, riser–seabed interaction, local flexure, fatigue damage*

## 1 Introduction

Unbonded flexible riser has been used in the offshore oil and gas transportation from seabed well to floating structure since 1970s [1]. It is a kind of complicated composite structure consisting of several concentric layers, see Fig. 1. Due to the special construction, unbonded flexible riser can undergo large bending deformation without compromising the axial strength and pressure integrity. Therefore, it is often preferentially considered for the application in deep and ultradeep water. However, the complicated construction significantly increases the assessment challenge of ultimate strength and fatigue damage, thus attracting attention from researchers.

The analytical approach is a technically feasible and computationally efficient method and extensively applied to investigate the unbonded flexible riser behavior performance. The carcass armor and pressure armor are interlocked structures and can be treated as orthotropic cylinders [2–4]. As for the helical wire layers, they significantly contribute to the axisymmetric and bending nonlinearity of the flexible riser, thus becomes the research focus [5–10]. Roberto and Celso [11] and Bahtui et al. [12] analytically investigated the axisymmetric and bending behavior of flexible riser considering the effect of the helical wire. Alfano et al. [13] and Bahtui et al. [14] proposed a constitutive model for flexible riser in the framework of an Euler–Bernoulli beam model. In this model, the stress–strain relationship is obtained by treating the frictional sliding of adjacent layers in flexible riser as the frictional sliding of microplanes in a continuum medium.

Except for better understanding the axisymmetric and bending behavior of flexible riser, the extensive investigation of analytical approach also aims to investigate the fatigue damage of helical wire, since it is one of the critical components prone to fatigue failure. Sævik [15] proposed two theoretical models which applied

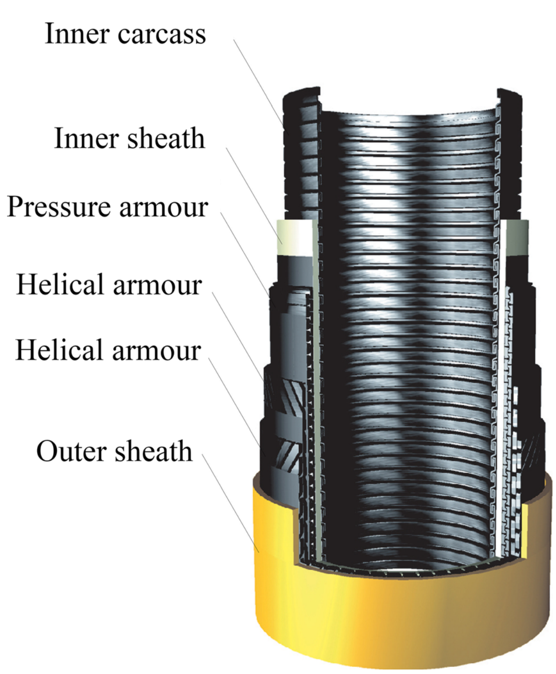


**Fig. 1 Typical flexible riser components**

[1]Corresponding author.

Contributed by the Ocean, Offshore, and Arctic Engineering Division of ASME for publication in the JOURNAL OF OFFSHORE MECHANICS AND ARCTIC ENGINEERING. Manuscript received June 22, 2016; final manuscript received April 20, 2017; published online May 25, 2017. Assoc. Editor: Luis V. S. Sagrilo.

nonlinear bending moment–curvature relationship and sandwich beam theory, respectively, to describe the sticking–sliding behavior of helical wire and verified them against the experimentally obtained fatigue damage data. de Sousa et al. [1] applied the in-house tool, ANFLEX, to calculate the global response of a catenary flexible riser and then used a developed code to transport the global response to the local model for the stress assessment of helical wire. The results in Ref. [1] indicated the touchdown point (TDP) is also one of the critical positions for catenary flexible riser as well as steel catenary riser.

The purpose of this study is to investigate the fatigue damage of helical wires in catenary flexible riser near TDP based on an analytical model of flexible riser. This model treats the axisymmetric and bending behavior separately. The axisymmetric formulation takes into account the interlayer interaction by setting radial interlayer dummy spring with stiffness varying based on the interlayer penetration and separation condition. In the bending formulation, the helical wire axial stress is traced to calculate the axial force gradient, which combined with the interlayer pressure obtained from axisymmetric formulation is applied to determine the sliding region. Based on the sliding region, the bending stiffness can be calculated directly. This model is implemented into finite element (FE) software, ABAQUS by using subroutine UEL for the global analysis of the flexible riser. To simulate the riser–seabed interaction, a linearly hysteretic seabed model [16,17] is applied. Finally, parametric analyses in the installation plane are carried out to demonstrate the sensitivity of fatigue damage of helical wire near TDP to the seabed stiffness and interlayer friction.

## 2 Flexible Riser Model

In this study, the layers of the flexible riser are analyzed separately with the same axial displacement $u_z$, axial rotation $\phi_z$, the bending $\phi_x$ about $x$-axial, and $\phi_y$ about $y$-axial, but different radial displacement $u_r$, see Fig. 2. This model is established based on the following assumptions:

(1) The helical wire only slide along its axial direction, i.e., the loxodromic curve [15].
(2) The curvature is constant along the flexible riser element.
(3) The interlayer contact pressure results from axisymmetric response and remains constant during bending behavior.
(4) The sliding friction is equal to the maximum static friction.
(5) Initial state of helical wire is approximately stress-free.

### 2.1 Analytical Formulation

*2.1.1 Axisymmetric Formulation.* The axisymmetric loads include the axial tension, torque, internal, and external pressure. To solve the displacements under these loads, the equilibrium equation should be established. de Sousa et al. [2] proposed an effective approach to simplify the carcass armor and pressure armor into equivalently orthotropic cylinder. Therefore, the flexible riser layers can be divided into two categories: cylindrical layer and helical wire layer. For the sake of saving space, the equivalent method would not be detailed in the present study.

As for the cylindrical layer, the stress–strain relationship can be expressed as follows:

$$\begin{Bmatrix} \sigma_1 \\ \sigma_2 \\ \sigma_{12} \end{Bmatrix} = \begin{bmatrix} \dfrac{E_1}{1-\nu_{12}\nu_{21}} & \dfrac{\nu_{12}E_1}{1-\nu_{12}\nu_{21}} & 0 \\ \dfrac{\nu_{21}E_2}{1-\nu_{12}\nu_{21}} & \dfrac{E_2}{1-\nu_{12}\nu_{21}} & 0 \\ 0 & 0 & G_{12} \end{bmatrix} \begin{Bmatrix} \varepsilon_1 \\ \varepsilon_2 \\ \gamma_{12} \end{Bmatrix} \tag{1}$$

where the $E$, $v$, and $G$ are, in this order, the Young's modulus, Poisson's ratio, and shear modulus. The subscripts 1 and 2 represent the axial and circumferential directions, respectively. For the isotropic layer, $E_1$ is equal to $E_2$, and $\nu_{12}$ is equal to $\nu_{21}$.

The axisymmetric strains of cylindrical layer are described by the following equations [18]:

$$\varepsilon_1 = \frac{u_z}{L} \quad \varepsilon_2 = \frac{u_r}{R} \quad \gamma_{12} = R\frac{\phi_z}{L} \tag{2}$$

where $L$ and $R$ represent the length and radius of the cylinder.

As for the helical wire, the axial stress is expressed as follows [19]:

$$\varepsilon_{0X} = \frac{u_z}{L}\cos^2(\alpha) + \frac{u_r}{R}\sin^2(\alpha) + R\frac{\phi_z}{L}\sin(\alpha)\cos(\alpha) \tag{3}$$

where $\alpha$ is the lay angle of helical wire.

Under the axisymmetric loads, the treatment of the interlayer interaction should be elaborated. Witz and Tan [5] and Bahtui et al. [12] investigated interlayer interaction based on the structural continuity and equilibrium along radial direction. In this study, the interlayer interaction is modeled by setting up radial dummy springs between the medium surfaces of adjacent layers, see Fig. 3.

Based on the principle of virtual work, the strain energy $U$ and the work $W$ related with the external force are obtained as follows:

$$U = \sum_{i=1}^{\bar{N}} \iiint \left(\frac{1}{2}\{\boldsymbol{\sigma}_i\}^{\mathrm{T}}\{\boldsymbol{\varepsilon}_i\}\right) dV + \sum_{i=1}^{\bar{N}-1} \frac{1}{2} L k_i (u_{r,i} - u_{r,i+1})^2 \tag{4}$$

$$W = Fu_z + T\phi_z + \left[P_{\mathrm{in}}R_2^2\left(\frac{u_z}{L} + \frac{2u_{r,2}}{R}\right) - P_{\mathrm{out}}R_N^2\left(\frac{u_z}{L} + \frac{2u_{r,N}}{R}\right)\right]\pi L \tag{5}$$

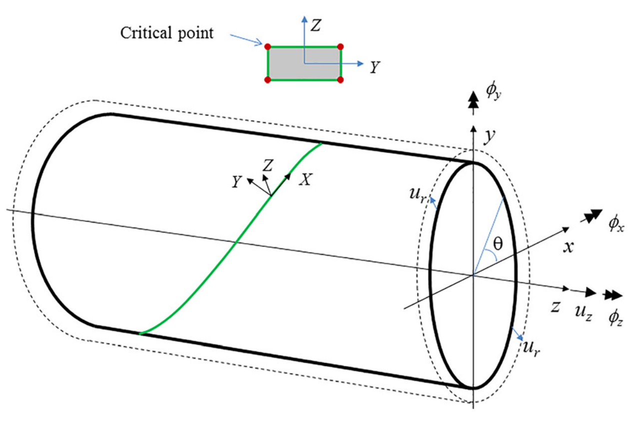


**Fig. 2 Displacement symbols of a layer and the critical point of helical wire**

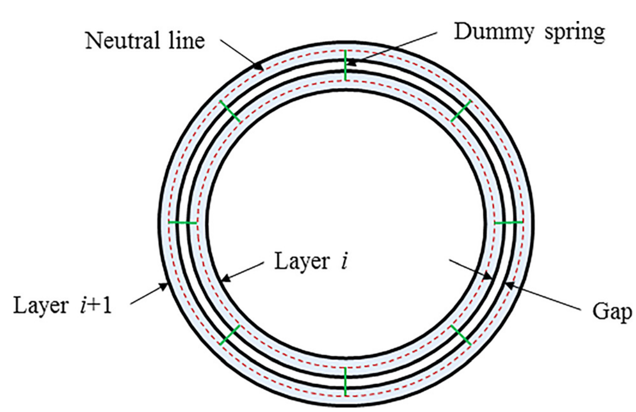


**Fig. 3 Sketch of interlayer interaction model**

where $\bar{N}$ is the number of layers, subscript $i$ represents the $i$th layer, $F$ and $T$ are the axial force and torque, respectively, and $P_{\text{in}}$ and $P_{\text{out}}$ are the internal and external pressure, respectively. For the cylindrical layer and helical armor, $\{\boldsymbol{\varepsilon}\} = \{\varepsilon_1, \varepsilon_2, \varepsilon_{12}\}^{\mathrm{T}}$ and $\{\varepsilon_{0X}\}$, respectively. $k_i$ is the stiffness of radial dummy springs between layers $i$ and $i+1$, which will be iteratively updated according to the interlayer penetration condition.

By letting $U = W$ and substituting Eqs. (1)–(3) into Eqs. (4) and (5), the equilibrium equation is established, based on which the axial force–elongation relationship reflecting the axial stiffness of the flexible riser can be calculated.

*2.1.2 Bending Formulation.* The bending stiffness of cylindrical layers can be easily obtained, so this section only focuses on the bending behavior of the helical armor. Due to the interlayer friction, the helical wires stick to the adjacent layer at the initial bending stage. When the curvature achieves to critical value [6], helical wire starts to slide from the neutral surface position. The sticking and sliding axial stresses induced by bending are given by [9]

$$\sigma_{0X} = \begin{cases} ER\cos^2(\alpha)\sin(\theta)\kappa & \text{Sticking} \\ (P_1 f_1 + P_2 f_2)\dfrac{R\theta}{\sin(\alpha)t} & \text{Sliding} \end{cases} \tag{6}$$

where $\kappa$ is the curvature, $\theta$ is angular position in the range $[0, \pi/2]$, see Fig. 2, $P_1$ and $P_2$ are the internal and external pressure of the helical armor, $f_1$ and $f_2$ are the corresponding friction coefficients, and $t$ is the layer thickness. This study takes the bending about $x$-axis as an example, so $\kappa$ is equal to $\phi_x/L$.

The sliding part of the helical wire keeps axial stress constant and would not contribute to the axial strain energy with curvature varying. Therefore, the equilibrium between work done by bending moment increment and the corresponding axial strain energy can be expressed as

$$\begin{aligned} \delta M_x \delta\phi_x &= \iiint_V E(\delta\varepsilon_{0X})^2 d\mathrm{v} \\ &= \int_0^L \int_{R-t/2}^{R+t/2} \left[ 4\int_{\theta_s}^{\pi/2} ER^2\cos^4(\alpha)\sin^2(\theta)\left(\frac{nb}{2\pi}d\theta\right)\right] dr \\ &\quad \times \frac{dl}{\cos\alpha}\left(\frac{\delta\phi_x}{L}\right)^2 \\ &= \frac{1}{2} n\mathrm{E}\mathrm{A}R^2\cos^3(\alpha)\left(1 - \frac{2}{\pi}\theta_s + \frac{1}{\pi}\sin(2\theta_s)\right)\frac{\delta\phi_x}{L}\delta\phi_x \\ &= EI_0\left(1 - \frac{2}{\pi}\theta_s + \frac{1}{\pi}\sin(2\theta_s)\right)\frac{\delta\phi_x}{L}\delta\phi_x \end{aligned} \tag{7}$$

Thus, the bending stiffness of helical armor is given by

$$\mathrm{EI} = EI_0\left(1 - \frac{2}{\pi}\theta_s + \frac{1}{\pi}\sin(2\theta_s)\right) \tag{8}$$

where $\delta M_x$ is the virtual bending moment increment, $[0, \theta_s]$ represents the sliding region along the circumferential direction, $EI_0$ is the nonsliding bending stiffness, and $n$ is the number of the helical wires in helical armor.

In this study, the axial stresses of helical wires along circumference are traced at each time step to determine the sliding region, and then the bending stiffness is calculated for the next time step according to Eq. (8). The sliding region can be determined based on the axial stress gradient

$$\begin{aligned} &\text{Sliding:} \quad \left| E\frac{d\varepsilon_{0X}}{dX}\bar{A}\right| \geq F_f \\ &\text{Sticking:} \quad \left| E\frac{d\varepsilon_{0X}}{dX}\bar{A}\right| < F_f \end{aligned} \tag{9}$$

where $F_f = (P_1 f_1 + P_2 f_2)b$ is the maximum static friction force per unit length of helical wire, $\bar{A}$ and $b$ are the cross-sectional area and width of helical wire, respectively. It should be noted that only the stresses at a quarter of the helical wire, i.e., $\theta \in [0, \pi/2]$, are traced, and thus, the present model is limited to two-dimensional analysis.

Previously obtained bending stiffness is just related to the axial behavior of helical wire. Dong et al. [20] investigated the contribution of the helical wire local flexure to the bending stiffness and derived the following expression:

$$EI_{\mathrm{bt}} = \frac{1}{2}n\left(EI_Z(1+\sin^2\alpha)\cos\alpha + EI_Y\cos^7\alpha + GJ\sin^2\alpha\cos\alpha^5\right) \tag{10}$$

where $I_Y$, $I_Z$, and $J$ are, in turn, the normal, transverse, and torsional moment of inertia, respectively. This expression is applied in the present study.

*2.1.3 Stress at Critical Point.* The stress at critical point of helical wire along $X$-axis taking into account the local flexure can be expressed as follows [19]:

$$\sigma_X = E(\varepsilon_{0X} + Y\kappa_Z + Z\kappa_Y) \tag{11}$$

where $\kappa_Y$ and $\kappa_Z$ are the local normal and transverse curvatures, respectively.

Axisymmetric response induced local flexures are given as follows [15]:

$$\begin{aligned} \kappa_Y &= -\frac{u_z}{L}\frac{\sin^2(\alpha)\cos^2(\alpha)}{R} + \frac{u_r}{R}\frac{\sin^2(\alpha)\cos^2(\alpha)}{R} \\ &\quad + \frac{\phi_z}{L}\left(2\sin(\alpha)\cos^3(\alpha) + \sin^3(\alpha)\cos(\alpha)\right) \\ \kappa_Z &= 0 \end{aligned} \tag{12}$$

As well as the research in Ref. [15], this study prescribes that the helical wire slides only along the loxodromic curve, and thus, the local flexures induced by bending response are given by

$$\begin{aligned} \kappa_Y &= \cos^4(\alpha)\sin(\theta)\kappa \\ \kappa_Z &= \cos(\alpha)(1+\sin^2(\alpha))\cos(\theta)\kappa \end{aligned} \tag{13}$$

**2.2 Implementation in ABAQUS.** Due to the nonlinear bending moment–curvature relationship, the flexible riser can be modeled in ABAQUS using the following methods: (*a*) beam element with nonlinear cross-sectional parameters which might be updated by user subroutine and (*b*) user-defined element based on UEL. This study utilizes two kinds of element to simulate the sticking–sliding zone of flexible riser. One is the usual beam element in ABAQUS with the flexible riser mass, axial stiffness of flexible riser obtained from axisymmetric formulation, and bending stiffness of the cylindrical layers. Another is user-defined element to simulate the bending stiffness of helical wires, called user-defined bending stiffness element. The two elements are both two-node element and share the same nodes.

At the end of each time step, the curvature and axial force of the beam element are extracted to calculate the interlayer pressure and the stress of helical wire, which are utilized to determine the sliding region. Next, the bending stiffness of helical wires is obtained for the next time step according to Eqs. (8) and (10).

## 3 Riser–Seabed Interaction Model

In this study, the linear hysteretic model [16,17] is applied to simulate the riser–seabed interaction, see Fig. 4. The relationship between penetration $d$ and resistance $P$ of point 1 can be described using the following equation governing the initial penetration:

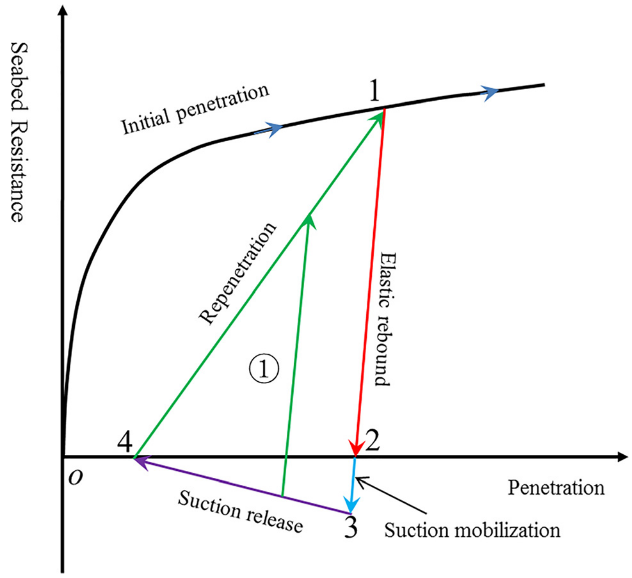


**Fig. 4 Linear hysteretic riser–soil interaction model**

$$P = N_P D(S_0 + S_g d) \quad N_P = a(d/D)^b \tag{14}$$

where $S_0$ and $S_g$ are mudline shear strength and shear strength gradient, respectively, $N_p$ is a dimensionless bearing factor, and $a$ and $b$ are empirical parameters taken to be 6.7 and 0.254, respectively [21].

As the riser uplift, the seabed resistance would decrease sharply from points 1 to 2, and then change to the clay suction, which mobilizes from points 2 to 3 and releases from points 3 to 4. If riser reverses to move downward during the suction release stage, the seabed resistance–penetration relationship would follow the line ① with the slope of elastic rebound curve. This model uses several parameters to determine the key points 3 and 4: $\lambda_{\rm suc}$ and $f_{\rm suc}$ are the penetration and suction factors at point 3; $\mu_{\rm sep}$ is the riser–seabed separation factor at point 4. This linear hysteretic interaction model is also implemented into ABAQUS by creating single-node element based on UEL, called user-defined touchdown element. This study takes $\lambda_{\rm suc}$, $f_{\rm suc}$, and $\mu_{\rm sep}$ to be 0.8, 0.2, and 0.6, respectively.

## 4 Validation and Case Study

**4.1 Validation of Flexible Riser Model.** Witz [22] experimentally studied the tension–elongation and bending moment–curvature relationships by using a 2.5-in unbonded flexible pipe. The present study employs this case to validate the analytical model. The friction coefficient between steel armor and antifriction armor is taken to be 0.1 [9].

Figure 5 demonstrates that the predicted axial force–elongation relationship is linear, and is very close to the mean value obtained by different institutes [22]. Compared with the experimental data, the proposed model fails to capture the hysteretic phenomenon but well predicts the axial behavior at large elongation. Figure 6 shows the bending moment–curvature relationship under internal pressure of 30 MPa. It is seen that the numerically predicted hysteretic loop well coincides with the experimental data. Overall, the proposed model can reasonably describe the axial and bending behavior of unbonded flexible riser.

The stress at critical point of helical wire is highly concerned in the fatigue assessment of flexible riser. Figure 7 demonstrates the comparison of the axial stress calculated from the present model and the detailed finite element model under initial contact pressure [23]. It can be seen that under the bending moment of 140 N·m, the helical wires keep full-sticking, and the result shows good agreement. When the bending moment reaches to 420 N·m, the helical wires partially slide in the detailed finite element model, but the present model predicts the helical wires full-sliding, thus gives larger axial stress near $\theta = \pi/2$. However, for the sliding part, the two models give similar result at the flexible riser middle part which the boundary constraint has little effect on. Equations (12) and (13) were employed to model the local flexure of helical wires in Ref. [15], where the numerically and experimentally obtained stress of helical wires showed good agreement. However, Tang et al. [24] indicated that Eq. (13) may overestimate the effect of the local flexure on the bending stress at critical point. The reason may be that Tang et al. [24] applied large curvature, $1\,{\rm m}^{-1}$, to the flexible riser, which may mitigate the local flexure due to the significantly lateral sliding. This study assumed that the two equations can reasonably consider the effect of the helical wire local flexure on the stress at critical point in global response of flexible riser.

Based on the present model, the stress at critical point under regular curvature response in the range $[-0.025\,{\rm m}^{-1}, 0.025\,{\rm m}^{-1}]$ is demonstrated in Fig. 8. Due to the consideration of local flexure, the stress would increase with relatively small slope after sliding occurs, and the slope increases with decreasing $\theta$.

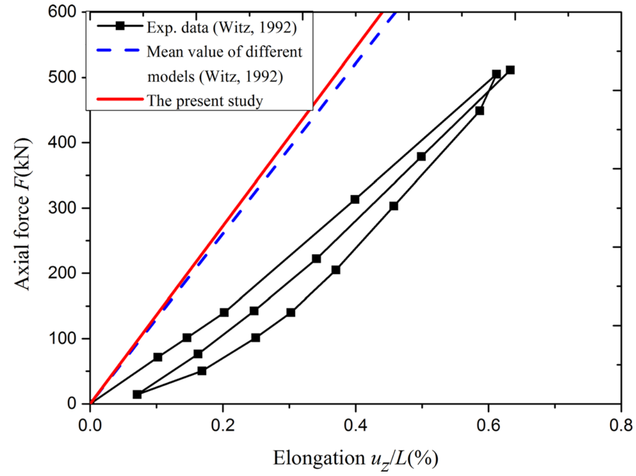


**Fig. 5 Relationship between axial force and elongation**

**4.2 Global Analysis of Flexible Riser.** Chen [25] reported the fatigue damage investigation of a 20-layer unbonded flexible pipe. Table 1 presents the main parameters. Based on the present model, the axial stiffness, the full-sticking bending stiffness, and

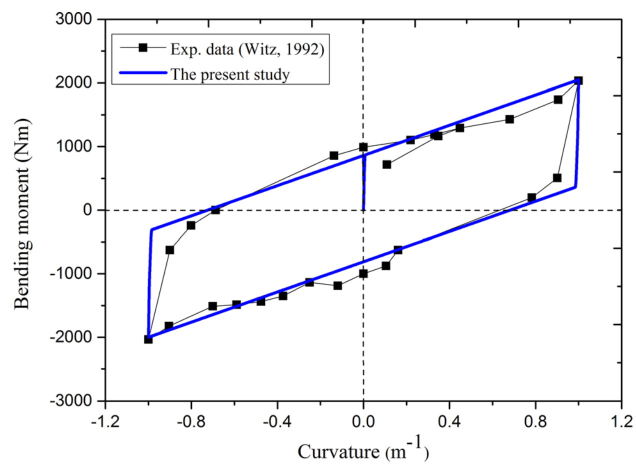


**Fig. 6 Relationship between bending moment and curvature**

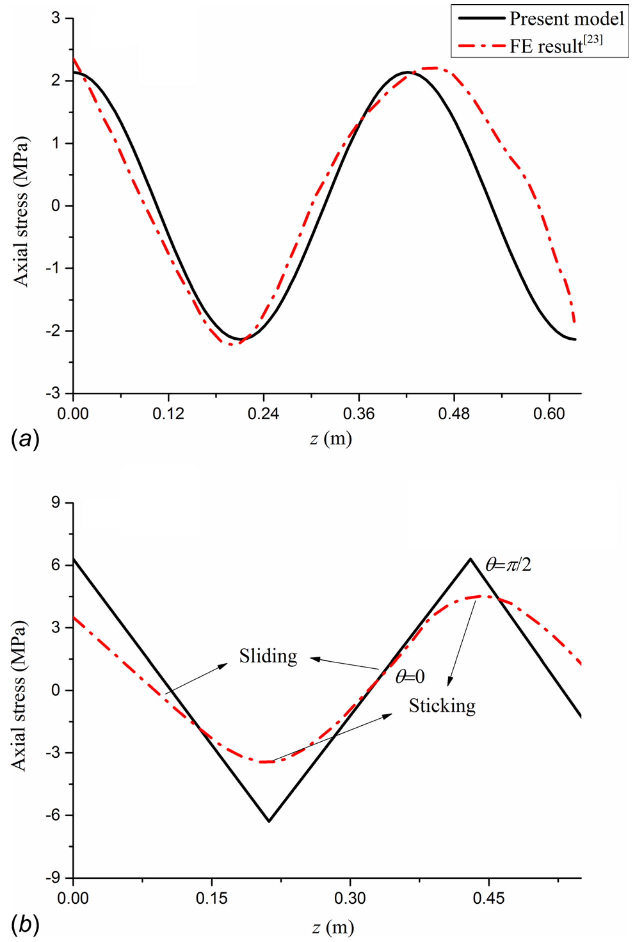


**Fig. 7 Axial stress obtained from the present model and FE result under different bending moment: (*a*) 140 N·m and (*b*) 420 N·m**

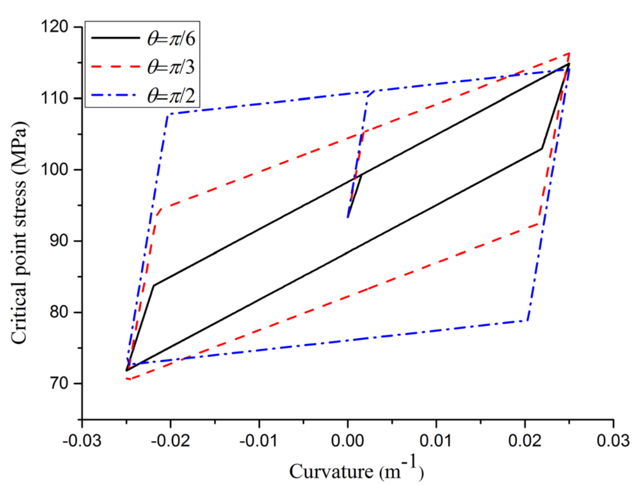


**Fig. 8 Relationship between critical point stress and curvature**

full-sliding bending stiffness can be calculated approximately equal to $7.17 \times 10^8$ N, $2.12 \times 10^7$ N·m$^2$, and $2.7 \times 10^5$ N·m$^2$, respectively. This study employs a flexible riser with the same construction to study the global performance of flexible riser. The flexible riser has a length of 1277.6 m and is installed in the sea area with water depth of 900 m for gas production. In this sea area, the wave trains follow Joint North Sea Wave Project (JONSWAP) spectrum. For simplification, the wave scatter diagram is concentrated to several blocks in which the center sea state with the combined occurrence probability is taken as the representative. The sea state parameters and current distribution are presented in Tables 2 and 3, respectively.

The user-defined bending stiffness element is used to model the bending stiffness variation of the sticking–sliding zone with length of about 150 m near TDP, see Fig. 9. Full-sticking is assumed for the rest where small curvature may occur. In this section, the following wave parameters and seabed parameters are applied for case study: significant wave height $H_s = 3.2$ m, spectrum peak period $T_p = 9.5$ s; $S_0 = 1.5$ kPa, $S_g = 2.5$ kPa/m. The outer sheath may be damaged during the installation and operation [25], which may lead to the flooding of seawater. This study focuses on the fatigue damage of the helical wires under flooding condition. Therefore, the annulus is flooded by seawater, and the external pressure acts on the inner sheath. Noted that the external pressure is smaller than the operational internal pressure 50.07 MPa [25].

The sticking–sliding zone consists of 75 user-defined elements with number increasing from bottom. This study investigates the flexible riser response using three models: (1) the present model (sticking–sliding model), (2) full-sliding model, and (3) full-sticking model. The critical point stress of model (1) can be calculated during the global analysis. As regard to models (2) and (3), the curvature and axial force are first obtained from the global analysis, and then the previous analytical formulations are applied to calculate the critical point stress. Figure 10 shows the bending moment–curvature trajectory of the flexible riser at the tenth user-defined bending stiffness element. It can be seen that the user-defined bending stiffness element combining with usual beam element can well capture the nonlinearly hysteretic bending moment–curvature relationship. When the helical wires full slides, the bending moment–curvature relationship would follow the full-sliding curve with the slope equal to the bending stiffness of the cylindrical layers. Figure 11 demonstrates the curvature and critical point stress at $\theta = \pi/2$ of the flexible riser at the tenth and 13th user-defined bending stiffness elements, respectively. Due to the change of the bending stiffness, the curvature may significantly deviate from the initial value, see Figs. 11(*a*) and 11(*b*). However, the critical point stress does not increase significantly with increasing curvature for the sticking–sliding case, see Fig. 11(*c*). In addition, although the full-sliding case predicts significantly larger curvature variation than the sticking–sliding and full-sticking cases in Fig. 11(*b*), the difference of related critical point stress variation in Fig. 11(*d*) is not such obvious. The reason is that the stress variation is very small with varying curvature when sliding occurs as marked by circle *i*, which is discussed in Sec. 4.1.

Figure 12 illustrates the relationship between seabed resistance and riser penetration at the tenth user-defined bending stiffness element. The user-defined touchdown element well captures the mobilization and release of the clay suction. When the riser repenetrates the seabed bottom, i.e., point 1, the resistance and penetration relationship would follow the initial penetration curve. In a full loop, the maximum suction is approximately equal to 0.2 times maximum resistance as expected.

It should be mentioned that the employed riser has high self-weight, which leads to high axial force burdening the end fitting, see Fig. 13. In addition, for simplification, the bending stiffener is not included at top end, since this study focuses on the response behavior near TDP. Therefore, the bending moment is very small near top end. If the bending stiffener is considered, the stress of helical wire at top end would increase and even may cause fatigue failure, but it would not be investigated in this study.

## 5 Fatigue Analysis of Helical Wire Near Touchdown Point

**5.1 Methodology of Fatigue Analysis.** *S*–*N* curve is often applied to assess the structure fatigue damage. The annulus

Table 1 Main parameters of unboned flexible riser

| Layer no. | Layer type | Inner diameter (mm) | Thickness (mm) | Lay angle (deg) | $E$ (MPa) | $\nu$ | Weight (kg/m) |
|---|---|---|---|---|---|---|---|
| 1 | Carcass | 228.6 | 7 | 87.6 | $2.1 \times 10^5$ | 0.3 | 23.786 |
| 2 | Antifriction | 242.6 | 3 | — | 1516.9 | 0.45 | 4.097 |
| 3 | Inner sheath | 248.6 | 12 | — | 1516.9 | 0.45 | 17.389 |
| 4 | Antifriction | 272.6 | 1.015 | — | 1516.9 | 0.45 | 0.873 |
| 5 | Pressure armor | 274.63 | 12 | 85.6 | $2.1 \times 10^5$ | 0.3 | 68.762 |
| 6 | Flat spiral armor | 298.63 | 5.995 | 85 | $2.1 \times 10^5$ | 0.3 | 40.835 |
| 7 | Antifriction | 310.62 | 1.525 | — | 55.2 | 0.45 | 1.569 |
| 8 | Helical armor1 | 313.67 | 5.995 | 44 | $2.1 \times 10^5$ | 0.3 | 43.049 |
| 9 | Antifriction | 325.66 | 0.405 | — | 55.2 | 0.45 | 0.425 |
| 10 | Antifriction | 326.47 | 1.525 | — | 55.2 | 0.45 | 1.649 |
| 11 | Helical armor2 | 329.52 | 5.995 | −44 | $2.1 \times 10^5$ | 0.3 | 45.4 |
| 12 | Antifriction | 341.51 | 0.405 | — | 55.2 | 0.45 | 0.445 |
| 13 | Antifriction | 342.32 | 1.525 | — | 55.2 | 0.45 | 1.729 |
| 14 | Helical armor3 | 345.37 | 5.995 | 42 | $2.1 \times 10^5$ | 0.3 | 46.99 |
| 15 | Antifriction | 357.36 | 0.405 | — | 55.2 | 0.45 | 0.466 |
| 16 | Antifriction | 358.17 | 1.525 | — | 55.2 | 0.45 | 1.808 |
| 17 | Helical armor4 | 361.22 | 5.995 | −42 | $2.1 \times 10^5$ | 0.3 | 49.265 |
| 18 | Antifriction | 373.21 | 0.405 | — | 55.2 | 0.45 | 0.487 |
| 19 | Antifriction | 374.02 | 0.405 | — | 55.2 | 0.45 | 0.319 |
| 20 | Outer sheath | 374.83 | 12 | — | 55.2 | 0.45 | 15.312 |

Table 2 Sea state parameters

| Sea state no. | Significant wave height, $H_s$ (m) | Spectrum peak period, $T_p$ (s) | Occurrence probability |
|---|---|---|---|
| 1 | 0.5 | 6.0 | 0.08 |
| 2 | 1.4 | 7.5 | 0.19 |
| 3 | 2.3 | 7.5 | 0.41 |
| 4 | 3.2 | 9.5 | 0.17 |
| 5 | 3.8 | 9.5 | 0.10 |
| 6 | 4.5 | 10.5 | 0.05 |

Table 3 Current speed versus water depth

| Distance to seabed | Current speed |
|---|---|
| 900 | 1.10 |
| 859 | 0.84 |
| 628 | 0.19 |
| 0 | 0.03 |

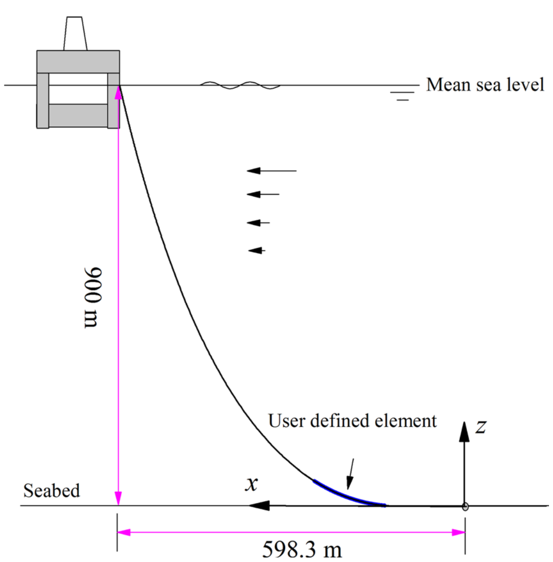


Fig. 9 Sketch of catenary flexible riser configuration

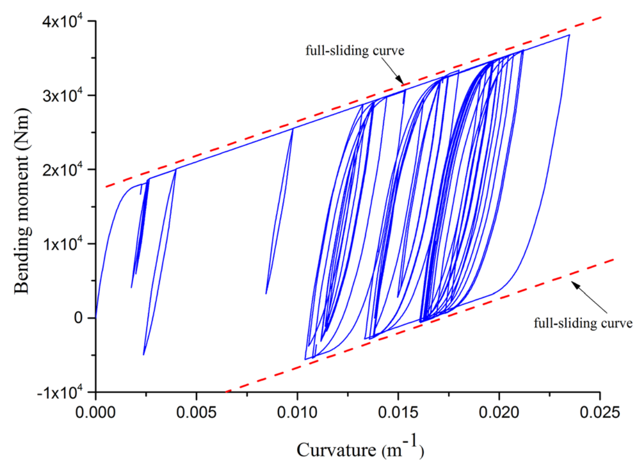


Fig. 10 Bending moment–curvature relationship at the tenth user-defined element of bending stiffness

condition of helical wire directly influences the choice of $S$–$N$ curve to be employed [1]. Helical wire of flexible riser is made of high strength steel, and the fatigue performance considering the presence of seawater can be given by [26]

$$\log N = \log A - m \log(\Delta\sigma) = 17.446 - 4.70 \log(\Delta\sigma) \qquad (15)$$

where $N$ represents the number of stress cycles the helical wire can withstand under the stress range of $\Delta\sigma$ MPa and $A$ and $m$ are material parameters. The stress cycles are extracted from the stress time history at critical point by using rain flow counting methodology. After obtaining the stress cycles, the Miner's rule [27] is applied to calculate the fatigue damage.

In this study, the global analysis of the flexible riser under short-term sea states in Table 2 are conducted, but only the case with wave and current aligned with positive $x$-axis (i.e., the installation plane) is considered since the heave motion of the vessel can lead to significant response of the catenary riser near touch-down point in the installation plane [28]. Next, the sensitivity of the fatigue damage of helical wire to angular position, seabed stiffness, and friction coefficient is in detail investigated. Meanwhile, the results are compared with those obtained from full-sticking and full-sliding models. The interlayer friction coefficients of the inner and outer surfaces are assumed to be the same.

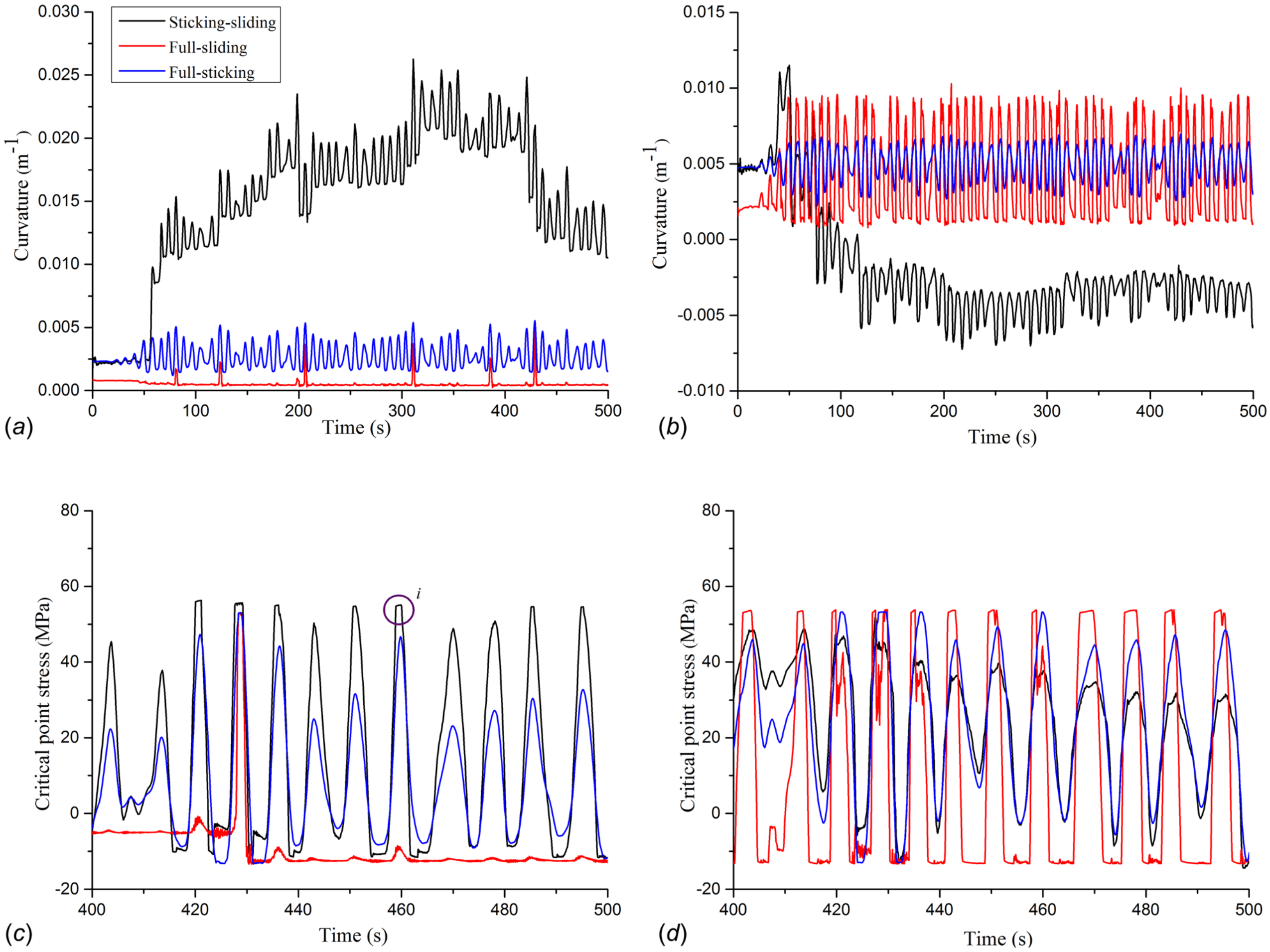


**Fig. 11 Time history of curvature and critical point stress: (*a*) and (*b*) are curvatures of the tenth and 13th user-defined bending elements, respectively; (*c*) and (*d*) are critical point stress at $\theta = \pi/2$ of the tenth and 13th user-defined bending elements, respectively**

Based on the global analysis in Sec. 4.2, the root mean squares of the stress at critical point corresponding to the simulation time of 3000 s, 5000 s, and 7000 s are calculated, and equal to 23.14 MPa, 24.42 MPa, and 23.95 MPa, respectively. Therefore, this study approximately considers that 3000 s simulation may give stability response and employs this simulation time in the following fatigue analyses.

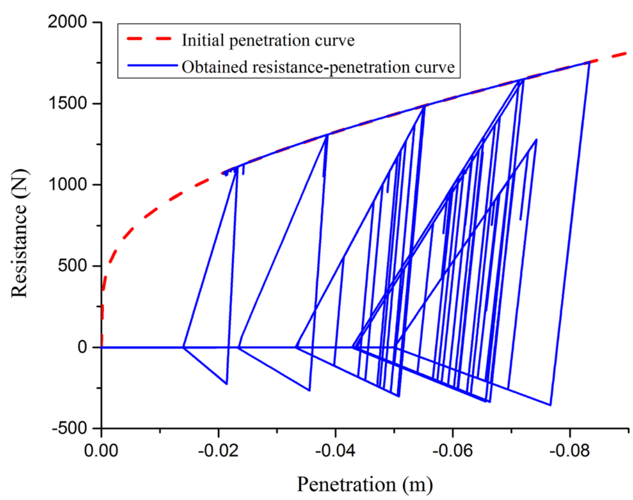


**Fig. 12 Resistance versus penetration at the tenth user-defined element of bending stiffness**

**5.2 Fatigue Damage at Different Angular Position.** The targeted flexible riser has four helical armor layers, and the calculation based on the present model indicates that the related interlayer pressure decreases from the inner to the outer under flooding condition. Figure 14 illustrates the fatigue damage of helical wire at different angular positions in the range [0, $\pi/2$]. For helical armor layers 1, 2, and 3, the fatigue damage increases with increasing $\theta$, while for helical armor layer 4, decreases with increasing $\theta$. This is because the interlayer pressure of the helical armor layer 4 is very small under the flooding condition, so the helical wire would slide at small curvature. After the sliding occurs, large $\theta$ corresponds to small ratio of stress to curvature, see Fig. 8. The helical armor layer 1 has the largest interlayer pressure, and thus, the stress would vary under the sticking condition in a very large curvature range. Therefore, this layer has the largest fatigue damage. Because the maximum fatigue damage occurs at $\theta = \pi/2$ of helical armor layer 1, the following study would take this position as the most critical position to study the fatigue damage features of the helical wires.

**5.3 Fatigue Damage Under Different Seabed Stiffness.** For steel catenary riser, high seabed stiffness may lead to high fatigue damage [29]. The full-sliding and full-sticking models give the same trend, as shown in Figs. 15(*a*) and 15(*b*). However, for the sticking–sliding model, the predicted maximum fatigue damage

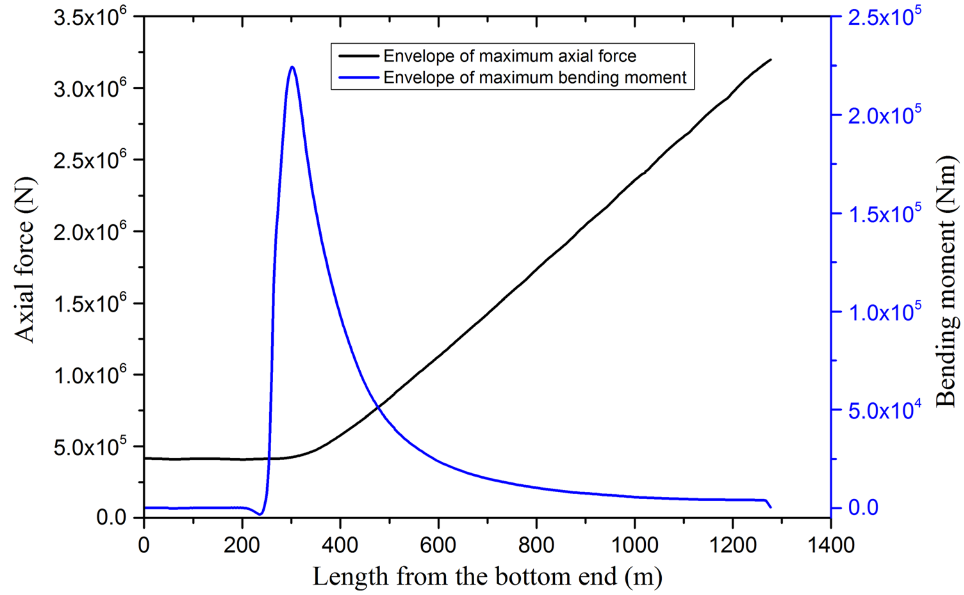


**Fig. 13 Envelope curves of the maximum axial force and bending moment**

near TDP increases, when $S_0$ increases from 1 kPa to 2.5 kPa, but the value at $S_0 = 3$ kPa is smaller than that at $S_0 = 2.5$ kPa, see Fig. 15(*c*). Therefore, the conclusion of high seabed stiffness corresponding to high fatigue damage may not apply to the unbonded flexible riser.

Traditional approach often applies elastic beam with constant stiffness to model unbonded flexible riser in the global analysis, and then calculates the critical point stress based on the axisymmetric and bending formulations [19]. This can significantly save the computational time. However, the predicted results may not be reasonable. Compared with the results obtained from sticking–sliding model, the full-sliding and full-sticking models would overestimate and underestimate the fatigue damage, respectively.

**5.4 Interlayer Friction Coefficient.** Interlayer friction has significant effect on the sliding curvature at which the helical wire starts to slide [19], thus affects the stress variation range. Figures 16(*a*) and 16(*b*) show that the fatigue damage obtained from full-sliding and full-sticking models increases with increasing friction coefficient $f_{\text{friction}}$. Full-sliding model obviously predicts higher fatigue damage than the full-sticking model, and large friction coefficient leads to large difference. When the coefficient increases from 0.15 to 0.20, the fatigue damage increment

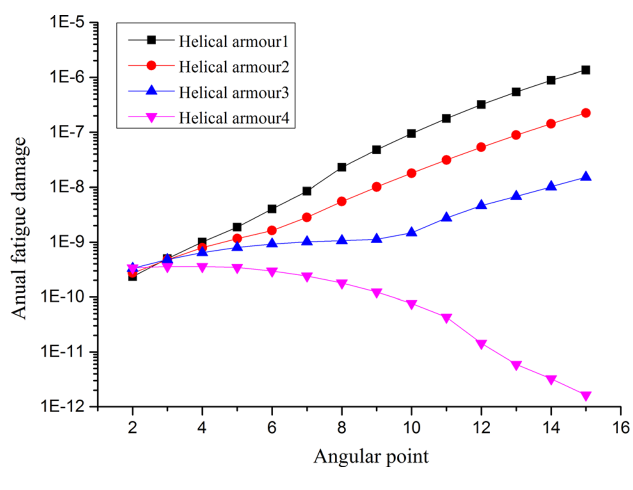


**Fig. 14 Fatigue damage at along the circumferential direction of different layers**

of the full-sliding model is very large. The reason is that the full-sliding model predicts large curvature variation, plus large friction coefficient corresponds to large sliding curvature, thus the stress would vary following the sticking stress based on Eq. (6) in a relatively large curvature range. As regard to the results of sticking–sliding model, the fatigue damage associated with friction coefficient of 0.15 is instead larger than that associated with friction coefficient of 0.20, see Fig. 16(*c*). This indicates that there may be not a certain law for the effect of the friction coefficient on the fatigue damage when considering the bending stiffness variation in the global analysis.

For conservatism, full-sliding model is often employed in the fatigue design of the flexible riser. However, the comparison between Figs. 16(*a*) and 16(*c*) indicates that full-sliding model overestimates the fatigue damage at friction coefficient of 0.10, 0.15, and 0.20, especially at 0.20, but underestimates the fatigue damage at friction coefficient of 0.05. Therefore, it is necessary to take into account the bending stiffness variation in the global analysis.

## 6 Conclusions

This study presents an analytical model to describe the axisymmetric and bending behaviors of unbonded flexible riser and implements it into the commercial software ABAQUS by using UEL to investigate the fatigue damage of helical wire in the catenary flexible riser near TDP. This model treats the axisymmetric and bending behaviors individually. The axisymmetric formulation takes into account the interlayer contact and separation by setting up dummy springs between adjacent layers. The spring stiffness would be updated according to the interlayer penetration and separation condition. After the iterative calculation of the axisymmetric formulation, the interlayer pressure can be obtained, and then is taken as input to the bending formulation to determine the sliding region of helical wires by comparing the maximum static friction and the helical wire axial force gradient. The sliding region is then applied to update the bending stiffness. In order to implement the analytical model into ABAQUS, this study takes the flexible riser as a combination of the usual beam element existing in ABAQUS and a user-defined element. The former has the same axial stiffness with the flexible riser and the same bending stiffness with the cylindrical layers, while the latter defines the bending stiffness of helical armor layers.

The present model is verified against test data in the literature, and both the axial force–elongation and bending moment–curvature

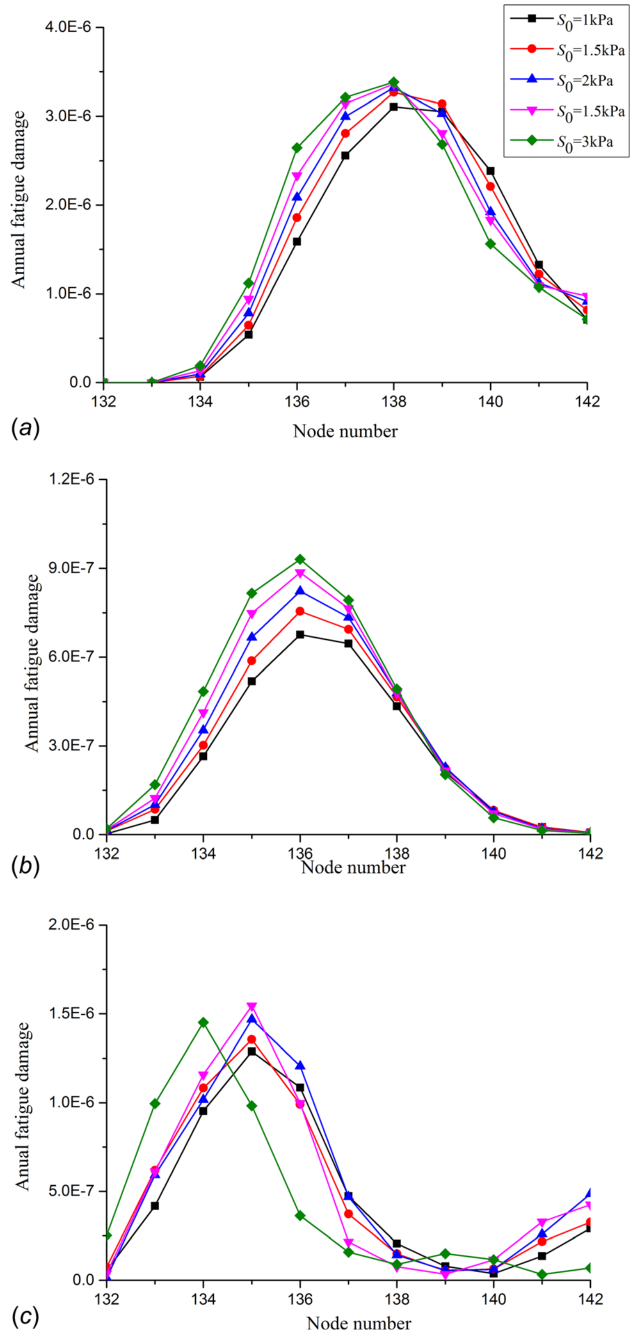


**Fig. 15 Fatigue damage versus seabed stiffness: (*a*) full-sliding, (*b*) full-sticking, and (*c*) sticking–sliding**

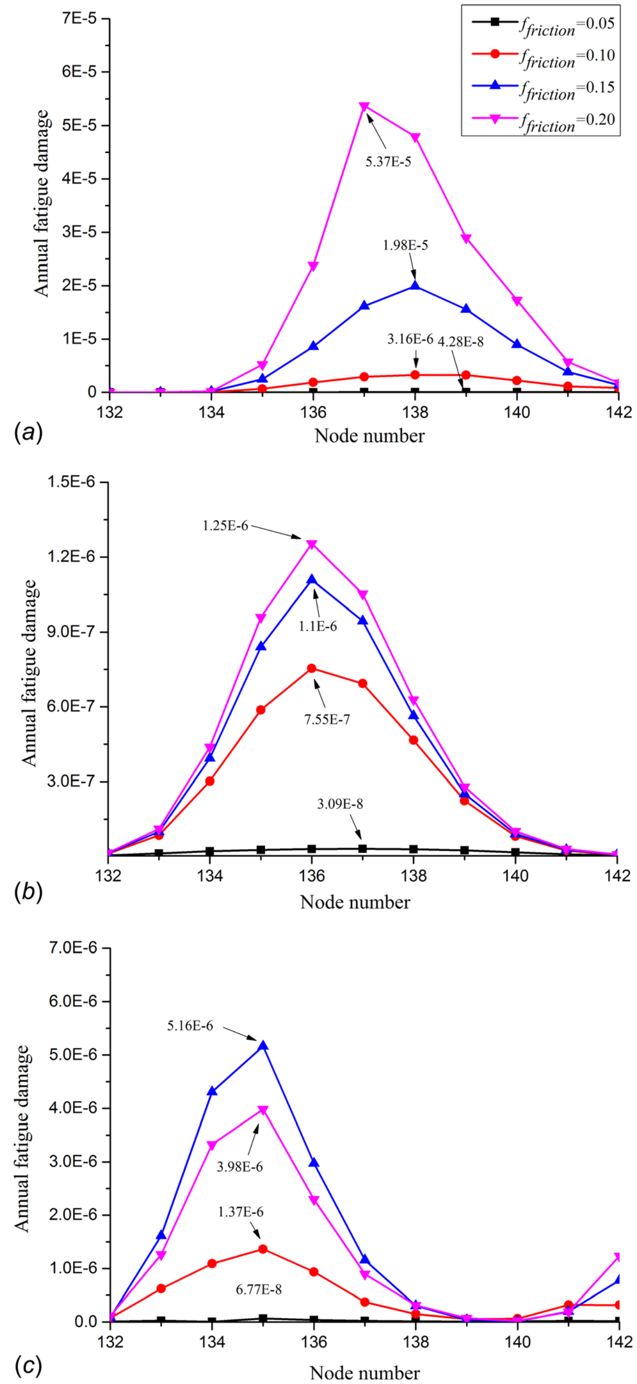


**Fig. 16 Fatigue damage versus friction coefficient $f_{\mathrm{friction}}$: (*a*) full-sliding, (*b*) full-sticking, and (*c*) sticking–sliding**

relationships show reasonable agreement. A case study of the targeted unbonded flexible riser is carried out in the installation plane under flooding condition. In the global analysis, the riser–seabed interaction is simulated by a linearly hysteretic seabed model. The result indicates that the user-defined element combined with usual beam element can well capture the hysteretic bending moment–curvature relationship under irregular response. Next, the sensitivity of the fatigue damage to the helical wire angular position, interlayer friction, and seabed stiffness are in detail investigated, and some conclusions are obtained:

(1) Under flooding condition, the innermost helical armor layer near TDP may be the critical layer prone to fatigue damage. For helical armor with large interlayer pressure, the most critical point is located at angular positon equal to $\pi/2$.

(2) For traditionally constant bending stiffness models, such as full-sliding and full-sticking models, high seabed stiffness and friction coefficient correspond to high fatigue damage. However, the law may not be suitable for the present flexible riser model considering the bending stiffness variation.

(3) Compared with the present sticking–sliding model, the full-sticking model may underestimate the fatigue damage near TDP, while the full-sliding model may overestimate the fatigue damage. For the present case, the full-sliding model gives too conservative prediction of fatigue damage at high friction coefficient.

In conclusions, the present model can reasonably simulate the unbonded flexible riser behavior in global analysis. For accurate fatigue damage prediction, the nonlinear bending stiffness should be taken into account.

## Acknowledgment

This paper is supported by the Natural Science Foundation of Jiangsu Province (Grant No. BK20160557), the General Program for Colleges and Universities in Jiangsu Province (Grant No. 16KJD570001), National Natural Science Foundation of China (Grant No. 51579146), and Shanghai Rising-Star Program (Grant No. 16QA1402300).

## References

[1] de Sousa, J. R. M., de Sousa, F. J. M., and de Siqueira, M. Q., 2012, "A Theoretical Approach to Predict the Fatigue Life of Flexible Pipes," J. Appl. Math., **2012**(6), pp. 1927–1936.
[2] de Sousa, J. R. M., Magluta, C., and Roitman, N., 2009, "On the Response of Flexible Risers to Loads Imposed by Hydraulic Collars," Appl. Ocean Res., **31**(3), pp. 157–170.
[3] de Sousa, J. R. M., Magluta, C., and Roitman, N., 2013, "A Study on the Response of a Flexible Pipe to Combined Axisymmetric Loads," ASME Paper No. OMAE2013-11384.
[4] de Sousa, J. R. M., Campello, G. C., and Kwietniewski, C. E. F., 2014, "Structural Response of a Flexible Pipe With Damaged Tensile Armor Wires Under Pure Tension," Mar. Struct., **39**, pp. 1–38.
[5] Witz, J. A., and Tan, Z., 1992, "On the Axial-Torsional Structural Behavior of Flexible Pipe, Umbilicals and Marine Cables," Mar. Struct., **5**(2–3), pp. 205–227.
[6] Witz, J. A., and Tan, Z., 1992, "On the Flexural Structural Behaviour of Flexible Pipes, Umbilicals and Marine Cables," Mar. Struct., **5**(2–3), pp. 229–249.
[7] Out, J. M. M., and von Morgen, B. J., 1997, "Slippage of Helical Reinforcing on a Bent Cylinder," Eng. Struct., **19**(6), pp. 507–515.
[8] Leroy, J. M., and Estrier, P., 2001, "Calculation of Stresses and Slips in Helical Layers of Dynamically Bent Flexible Pipes," Oil Gas Sci. Technol., **56**(6), pp. 545–554.
[9] Kraincanic, I., and Kebadze, E., 2001, "Slip Initiation and Progression in Helical Armouring Layers of Unbonded Flexible Pipes and Its Effect on Pipe Bending Behavior," J. Strain Anal., **36**(3), pp. 265–275.
[10] Østergaard, N. H., Lyckegaard, A., and Andreasen, J. H., 2012, "A Method for Prediction of the Equilibrium State of a Long and Slender Wire on a Frictionless Toroid Applied for Analysis of Flexible Pipe Structures," Eng. Struct., **34**(1), pp. 391–399.
[11] Roberto, R. J., and Celso, P. P., 2003, "A Consistent Analytical Model to Predict the Structural Behavior of Flexible Risers Subjected to Combined Loads," ASME J. Offshore Mech. Arct. Eng., **126**(2), pp. 141–146.
[12] Bahtui, A., Bahai, H., and Alfano, G., 2009, "Numerical and Analytical Modeling of Unbonded Flexible Risers," ASME J. Offshore Mech. Arct. Eng., **131**(2), p. 021401.
[13] Alfano, G., Bahtui, A., and Bahai, H., 2009, "Numerical Derivation of Constitutive Models for Unbonded Flexible Risers," Int. J. Mech. Sci., **51**(4), pp. 295–304.
[14] Bahtui, A., Alfano, G., and Bahai, H., 2010, "On the Multi-Scale Computation of Un-Bonded Flexible Risers," Eng. Struct., **32**(8), pp. 2287–2299.
[15] Sævik, S., 2011, "Theoretical and Experimental Studies of Stresses in Flexible Pipes," Comput. Struct., **89**(23–24), pp. 2273–2291.
[16] Wang, K. P., Xue, H. X., and Tang, W. Y., 2013, "Fatigue Analysis of Steel Catenary Riser at the Touch-Down Point Based on Linear Hysteretic Riser-Soil Interaction Model," Ocean Eng., **68**(4), pp. 102–111.
[17] Wang, K. P., Tang, W. Y., and Xue, H. X., 2015, "Time Domain Approach for Coupled Cross-Flow and In-Line VIV Induced Fatigue Damage of Steel Catenary Riser at Touchdown Zone," Mar. Struct., **41**, pp. 267–287.
[18] McNamara, J. F., and Harte, A. M., 1989, "Three Dimensional Analytical Simulation of Flexible Pipe Wall Structure," ASME J. Offshore Mech. Arct. Eng., **114**(2), pp. 69–75.
[19] Skeie, G., Sødahl, N., and Steinkjer, O., 2012, "Efficient Fatigue Analysis of Helix Elements in Umbilicals and Flexible Risers: Theory and Applications," J. Appl. Math., **2012**, p. 246812.
[20] Dong, L. L., Huang, Y., and Zhang, Q., 2013, "An Analytical Model to Predict the Bending Behavior of Unbonded Flexible Pipes," J. Ship Res., **57**(3), pp. 171–177.
[21] Aubeny, C. P., and Biscontin, G., 2009, "Seafloor-Riser Interaction Model," Int. J. Geomech., **9**(3), pp. 133–141.
[22] Witz, J. A., 1996, "A Case Study in the Cross-Section Analysis of Flexible Risers," Mar. Struct., **9**(9), pp. 885–904.
[23] Zhang, M. M., Chen, X. Q., Fu, S. X., Guo, Y. S., and Ma, L. X., 2015, "Theoretical and Numerical Analysis of Bending Behavior of Unbonded Flexible Risers," Mar. Struct., **44**, pp. 311–325.
[24] Tang, M. G., Yang, C., Yan, J., and Yue, Q. J., 2015, "Validity and Limitation of Analytical Models for the Bending Stress of a Helical Wire in Unbonded Flexible Pipes," Appl. Ocean Res., **50**, pp. 58–68.
[25] Chen, M. H., 2011, "Fatigue Analysis of Flexible Pipes Using Alternative Element Types and Bend Stiffener Data," M.Sc. thesis, Norwegian University of Science and Technology, Trondheim, Norway.
[26] DNV, 2010, "Fatigue Design of Offshore Steel Structures," Det Norske Veritas, Oslo, Norway, Standard No. DNV-RP-C203.
[27] Miner, M. A., 1945, "Cumulative Damage in Fatigue," ASME J. Appl. Mech., **12**(3), pp. 159–164.
[28] Passano, E., and Larsen, C. M., 2007, "Estimating Distributions for Extreme Response of a Catenary Riser," ASME Paper No. OMAE2007-29547.
[29] Randolph, M., and Quiggin, P., 2009, "Non-Linear Hysteretic Seabed Model for Catenary Pipeline Contact," ASME Paper No. OMAE2009-79259.